High-resolution whole-brain staining for electron microscopic circuit reconstruction

Shawn Mikula[1,2] & Winfried Denk[1,2]

Currently only electron microscopy provides the resolution necessary to reconstruct neuronal circuits completely and with single-synapse resolution. Because almost all behaviors rely on neural computations widely distributed throughout the brain, a reconstruction of brain-wide circuits—and, ultimately, the entire brain—is highly desirable. However, these reconstructions require the undivided brain to be prepared for electron microscopic observation. Here we describe a preparation, BROPA (brain-wide reduced-osmium staining with pyrogallol-mediated amplification), that results in the preservation and staining of ultrastructural details throughout the brain at a resolution necessary for tracing neuronal processes and identifying synaptic contacts between them. Using serial block-face electron microscopy (SBEM), we tested human annotator ability to follow neural 'wires' reliably and over long distances as well as the ability to detect synaptic contacts. Our results suggest that the BROPA method can produce a preparation suitable for the reconstruction of neural circuits spanning an entire mouse brain.

Large-scale neural circuit reconstruction is necessary for understanding how interacting neurons generate behavior[1,2]. However, the methods currently used to prepare tissue for electron microscopy with contrast and resolution sufficient to reliably identify all synapses and follow all neural wires are applicable to only relatively small samples[3–6]. This alone is an insurmountable obstacle to the reconstruction of larger circuits because dividing tissue before embedding would almost certainly cause enough damage along the plane of separation to make it impossible to follow thin processes from one piece to the next. Although the adult mouse brain can be stained in its entirety for electron microscopic observation using the wbPATCO (whole-brain periodic-acid–thiocarbohydrazide-OsO_4) protocol[7], this technique allows only myelinated axons to be followed reliably, and the preservation and contrast of membranes and small subcellular structures is insufficient to identify synapses unambiguously. The BROPA method presented here resolves these shortcomings: throughout the brain, the tissue ultrastructure was preserved well enough to identify chemical synapses and trace even the thinnest neurites, such as spine necks and small-caliber axons.

RESULTS

It has been shown that it is, in some cases, possible to equilibrate the substances involved in the preparation of whole brains for both light[8] and electron[7] microscopy by diffusion when using considerably extended incubation times. Although the ROTO (reduced-osmium staining followed by thiocarbohydrazide, TCH, amplification; **Fig. 1**) method yields excellent membrane contrast (**Supplementary Fig. 1b**) and preserves the subcellular ultrastructure very well[9,10], it does not provide usable staining beyond 200 µm in depth (**Fig. 1c** and **Supplementary Fig. 1a–e**). Large samples are, furthermore, disrupted mechanically, presumably owing to the formation of nitrogen bubbles during the amplification step (**Supplementary Fig. 2**). We determined that the reduced-osmium step is responsible for the limited penetration (data not shown) and reasoned that highly charged chemical species such as ferrocyanide, $Fe(CN)_6^{4-}$, are unable to cross lipid membranes and thus would have difficulty penetrating conventionally fixed tissue[11], which retains little if any extracellular space (ECS) as the cells swell from an osmotic imbalance that develops during aldehyde fixation[12,13]. To preserve the ECS, which is normally around 20% in living adult tissue[14] and provides long-range diffusion paths for hydrophilic solutes, we used a method[15] that corrects the osmotic imbalance by including membrane-impermeable solutes in the fixation medium.

Preserving the ECS improved stain penetration, but only slightly (**Fig. 1c** and **Supplementary Fig. 1f–i**). At a depth of a few hundred micrometers, a dark band developed where the ECS was reduced and was filled with an electron-dense substance (**Fig. 1d** and **Supplementary Fig. 1h**). This band formed over a range of OsO_4 concentrations (10–40 mM), even when the ECS fraction was increased beyond its value *in vivo*. The electron-dense substance is likely the result of some form of precipitation, as has been seen before for mixtures of $Fe(CN)_6^{4-}$ and OsO_4 (ref. 16). The band would then act as a barrier to the diffusion of some of the compounds involved. To find a solution to this problem, we varied many of the experimental parameters such as temperature, buffers and reducing agents used, and we included co-oxidants, organic solvents, chelators and detergents (see **Table 1**), in most cases without much effect.

In two cases we did, however, find a dramatic effect. Barrier formation was completely eliminated and staining became uniform

[1]Department of Biomedical Optics, Max Planck Institute for Medical Research, Heidelberg, Germany. [2]Present address: Electrons – Photons – Neurons, Max Planck Institute for Neurobiology, Martinsried, Germany. Correspondence should be addressed to S.M. (mikula@neuro.mpg.de).

RECEIVED 17 DECEMBER 2014; ACCEPTED 11 MARCH 2015; PUBLISHED ONLINE 13 APRIL 2015; DOI:10.1038/NMETH.3361

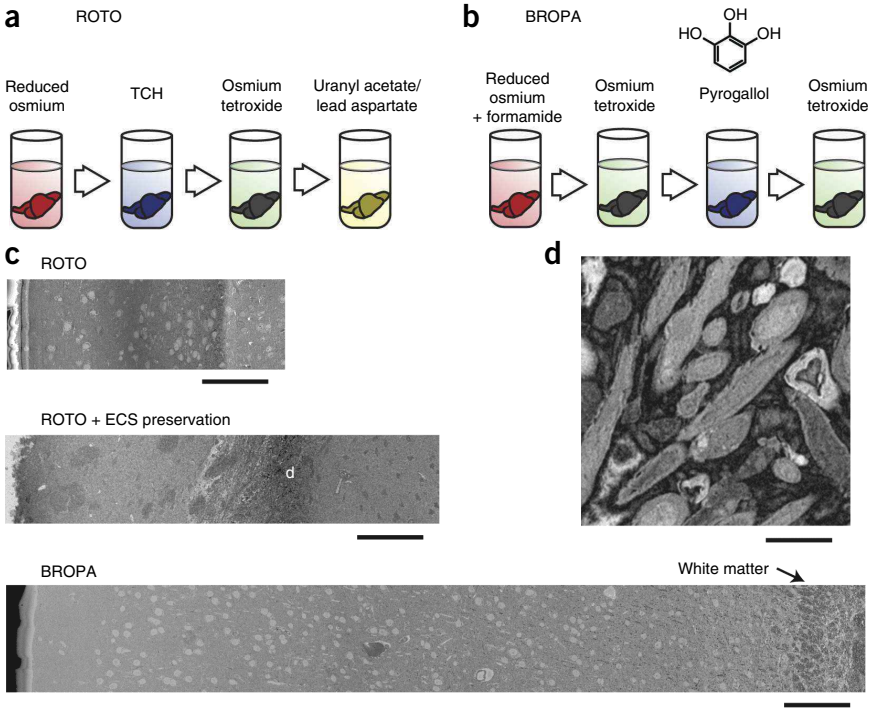

Figure 1 | BROPA overcomes stain-penetration limitations for reduced-osmium staining. (**a**,**b**) Sequence of steps for the reduced osmium–thiocarbohydrazide–osmium (ROTO) protocol (**a**) and the BROPA protocol (**b**). (**c**) SEM scans (440-nm pixel size, 2.8 kV, 100 pA, 0.0064 e^-/nm^2) of pieces of tissue prepared using ROTO under conditions that do not (top) and do (center) preserve the ECS and were taken from cortex and striatum, respectively, and of the cortex (bottom) in a BROPA-prepared whole brain (WB104). (**d**) High-resolution image of the dark-band region in the ECS sample (**c**, center). Scale bars, 100 µm (**c**) and 1 µm (**d**).

throughout the brain when either formamide or glycerol was included in the reduced-osmium solution (**Fig. 1b**,**c**). Of the two, formamide gave a considerably higher membrane contrast, comparable to that obtained with the standard reduced-osmium protocol[17] (data not shown). Formamide and glycerol are both polar protic solvents; therefore, we tried a number of other solvents that came from this class and that were structurally similar to either formamide (acetamide, formic acid and *N*-methylformamide) or glycerol (ethylene glycol and 1,2-propanediol) but found that none of them had any discernible effect on penetration (data not shown).

The mechanism by which formamide acts is unknown. It might prevent precipitation by generally solubilizing compounds[18], thereby avoiding barrier formation. It might also allow highly charged molecules to cross membranes. The latter possibility is supported by the observation (data not shown) that in the presence of formamide, ECS preservation is not necessary for uniform brain-wide staining. We also observed that increasing the $Fe(CN)_6^{4-}$ concentration required a corresponding increase in formamide concentration for complete and uniform staining (data not shown). When we tried very high concentrations of formamide (>50% v/v), we found sample expansion and reduced contrast but no significant effect on ultrastructural preservation.

The second obstacle to ROTO-based whole-brain staining is extensive damage caused by bubble formation (**Supplementary Fig. 2**), likely due to liberation of N_2 from tissue-bound TCH. Stain amplification, as provided by the TCH step in the ROTO protocol, is of paramount importance in situations that rely on a high stain density in the block. An example is serial block-face imaging[6,19], where imaging precedes cutting and the whole process occurs in vacuum, both all but precluding the intensification of the stain after a section is cut. We therefore searched for an alternative to TCH and first collected a list of compounds that had been shown to be osmiophilic[20]. When we inspected this list, it became apparent that these compounds are all reducing agents that react with OsO_4 via one of a small number of functional groups (hydrazines—which liberate N_2—thiols or thiones, alkenes, aromatic polyhydroxyls and aminohydroxyls, heterocyclic amines and primary amines; see Online Methods). We, therefore, added to our list other compounds containing at least one of these functional groups, excluding compounds that had a high molecular weight (>1,000 Da) or were water insoluble. By screening the resulting library of 40 compounds (**Table 2**), we found that replacing TCH by pyrogallol (1,2,3-trihydroxybenzene) resulted in the best preparations, an assessment taking into account membrane contrast and the presence of any signs of mechanical disruption, as well as stain penetration and uniformity.

When examining BROPA-prepared brains in cross-section (**Fig. 2a**) by scanning electron microscopy (SEM) and throughout small test volumes with SBEM (**Supplementary Videos 1–3**), we

Table 1 | Parameters varied to improve reduced-osmium sample penetration

Parameter	Values
Temperature	3, 20 and 50 °C
pH	3–12
Incubation time	1, 2, 4, 8, 24, 48, 72 and 96 h
Ferrocyanide	6, 12, 24, 35 and 70 mM
Osmium tetroxide	5, 10, 20, 40, 60 and 80 mM
Cacodylate buffer	0, 0.05, 0.1, 0.15 and 0.2 M
Primary oxidant	MnO_4^-, RuO_4 and $Cr_2O_7^-$
Alternate co-oxidants or redox reagents	Sodium ferrocyanide, ammonium ferrocyanide, potassium ferricyanide and potassium iodide
Alternate buffers	Phosphate, Tris, PIPES, Ringer's, borate, bicarbonate and *sym*-collidine
Polar protic solvents	Methanol, ethanol, 1- and 2-propanol, 1-, 2- and *tert*-butanol, acetic acid, ethyl acetate, formamide[a], formic acid, *N*-methylformamide, glycerol[a], 1,2-propanediol, ethylene glycol and ammonia
Polar aprotic solvents	Acetone, acetonitrile, dimethylformamide, dimethylacetamide, dimethylsulfoxide, tetrahydrofuran and pyridine
Detergents	Deoxycholic acid, sodium dodecylbenzenesulfonate, Triton X-100, Triton X-114 and Triton X-405, saponin and Tween
Chelators	Ethylenediamine, citrate, EDTA and EGTA
Polyhydric alcohols	Arabitol, mannitol and inositol

[a]Allowed for uniform staining.

Table 2 | Substitutes for thiocarbohydrazide to avoid damage from bubble formation during staining amplification

Functional class	Chemical name
Hydrazines	Semicarbazide, carbohydrazide, hydrazine hydrate and thiosemicarbazide
Organosulfur compounds	Thiourea, thioglycolic acid, 1,2-benzenedithiol, cysteine, methionine and thiophene
Aromatic polyhydroxyls	Tannic acid, pyrogallol[a], gallic acid, phloroglucinol, caffeic acid, catechol, resorcinol, hydroquinone and alizarin
Alkenes	Allyl alcohol and beta-carotene
Heterocyclic amines	Phenidone, pyrrole, histidine, 1,2,3-triazole, 1,2,4-triazole and 4-amino-4*H*-1,2,4-triazole
Primary amines	*o*-, *m*- and *p*-phenylenediamine, lysine, aniline, ethanolamine and 3,3-diaminobenzidine
Aromatic aminohydroxyls	2-, 3- and 4-aminophenol, amidol, metol and 4-hydroxyphenylglycine

[a]Resulted in the best preparations as determined by membrane contrast, signs of mechanical disruption, and stain penetration and uniformity.

found that all examined regions were largely free of most commonly observed sample preparation artifacts (**Fig. 2b**–**g**), such as varying membrane contrast, extracted or exploded mitochondria, crenellation of myelin sheaths or neurites, myelin 'figures' and heavy-metal precipitates[21]. Neurites never appeared completely ruptured, but membranes still occasionally contained holes a few hundred nanometers in size. The BROPA method yielded samples that could be imaged with SEM under high-vacuum conditions (**Fig. 2b**–**g**). Charging artifacts were absent when using either a coaxial silicon-junction detector, sensitive to backscattered electrons (**Fig. 2b**–**g**), or a side-mounted Everhart-Thornley detector (ETD; data not shown), sensitive to secondary electrons (SEs). Some residual conductivity is presumably provided by electrically conducting lower-oxidation-state osmium oxides[22]. We could not, however, obtain satisfactory images from uncoated samples using the in-lens SE detectors in either a single-beam SEM (Zeiss Merlin) or a prototype multibeam instrument[23] (Zeiss, mSEM) owing to charging inside of cell nuclei and in the lumen of blood vessels (data not shown). This behavior is consistent with that observed for smaller tissue samples prepared using the ROTO method[4,10,24]. The reason that ETDs and in-lens detectors give different results may be that (because of the electron-optical design of the Merlin) most of the low-energy SEs are directed into the column, thus leaving for the ETD only the more energetic SEs, which are less sensitive to the electric fields that arise as a result of charging. Coating the samples with a thin layer of palladium[24], in fact, resolved the artifacts seen when using the in-lens SE detector, and images could be taken with the mSEM (**Supplementary Fig. 3**). None of the images (**Figs. 2**–**4** and **Supplementary Videos 1**–**3**) taken from various regions of BROPA-prepared brains showed evidence of incomplete epoxy polymerization, such as poor cutting. This indicates that not only the staining steps but also the dehydration and infiltration steps were long enough for a sufficient equilibration of the substances involved.

To test whether a BROPA-prepared brain could form the basis for the connectomic reconstruction of an entire mouse brain, we evaluated synapse detectability and error rates for the manual reconstruction of neurites. To quantify synapse detectability, we selected a SBEM stack taken from the striatum (**Supplementary Video 1**) and traced 25 neurites that had been randomly selected among those that passed through the central region of the stack. For further analysis we chose the most highly branched among those neurites that, on the basis of its morphology and high spine density, was likely the distal dendrite of a medium spiny neuron. A trained annotator performed a full volume annotation (segmentation; **Fig. 3a**), then tried to identify all incident synapses and, finally, volume-labeled the corresponding presynaptic boutons (**Fig. 3a**–**c** and **Supplementary Data**). Two further annotators independently tried to identify all synapses incident upon the same piece of neurite and found, in addition to all 74 initially identified synaptic contacts, a number of synapses (ten in total, eight in common between the secondary annotators; **Fig. 3e**) that had not been detected by the first annotator. These synapses had smaller contact areas and fewer vesicles. One of these synapses had a contact that was average in size but was oriented almost perfectly in parallel to the cutting plane, which made its detection difficult. Some synapses could be identified easily from single cross-sectional images by the presence of both a postsynaptic density (PSD) and a vesicle cloud. We found that the mere presence of a PSD is highly predictive of a true synaptic contact because we never saw a clearly visible PSD whose corresponding presynaptic membrane did not also contact a vesicle cloud somewhere when we inspected the entire contact in three dimensions (using the image stack). In cases where it was unclear whether there was a PSD, we scored a contact as synaptic only when there was also a vesicle cloud touching the location in question (**Fig. 3b**,**c**). PSDs were generally

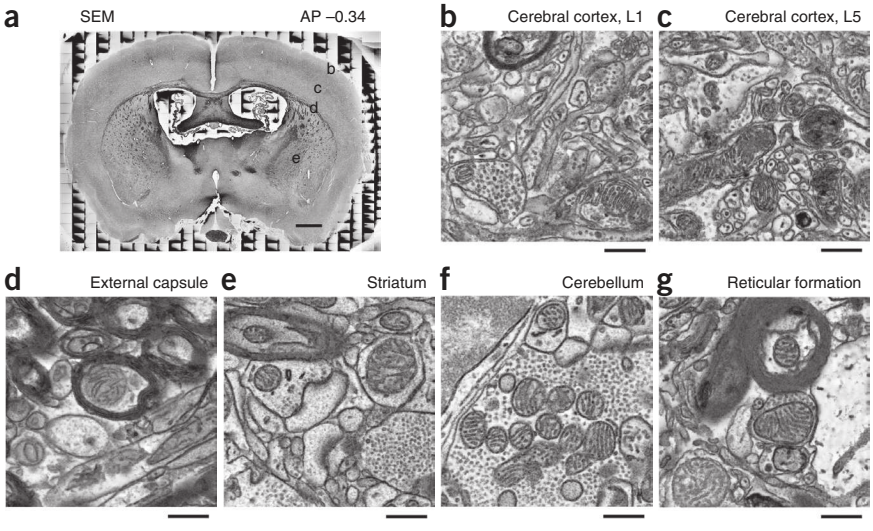

Figure 2 | Tissue ultrastructure is preserved well throughout BROPA-prepared brains. (**a**) Coronal block-face SEM image (440-nm pixel size, 4 kV, 150 pA, 0.0097 e^-/nm^2) of a whole mouse brain prepared using BROPA, cut at 0.34 mm posterior to bregma. The regular background pattern is due to epoxy charging. (**b**–**g**) High-magnification SEM images of various regions of the same brain (5-nm pixel size, 2.8 kV, 300 pA, 600 e^-/nm^2). **b**–**e** are taken from the same block face shown in **a**, where locations are indicated by the corresponding letters. Scale bars, 1 mm (**a**) and 500 nm (**b**–**g**).

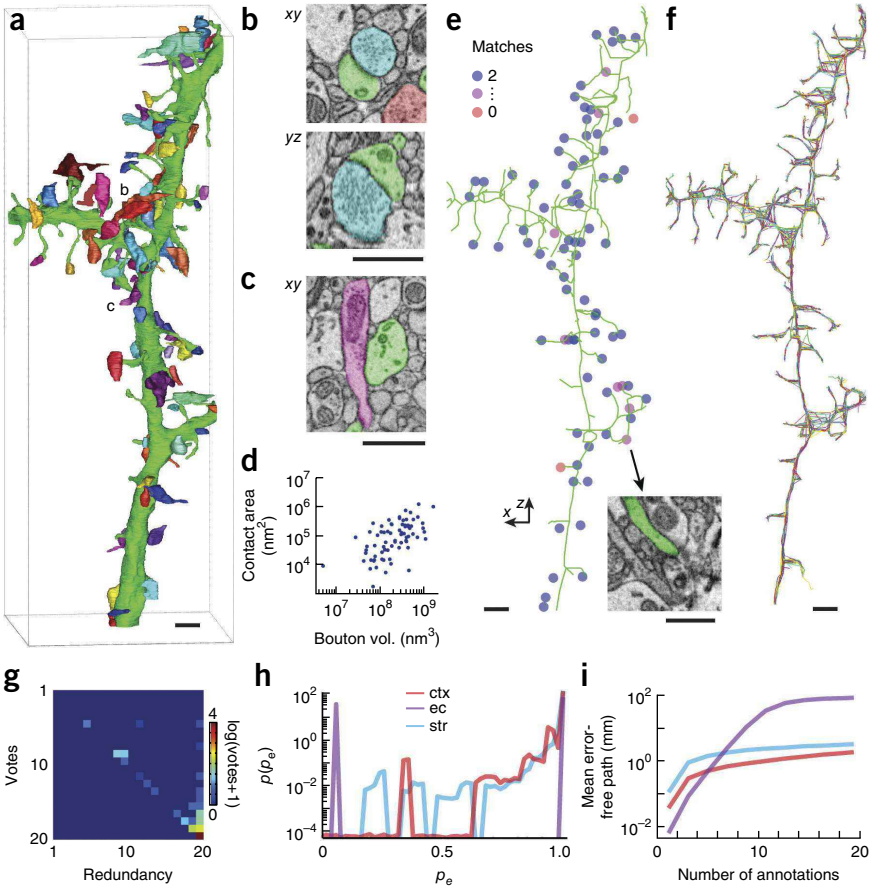

Figure 3 | BROPA-prepared brains allow reliable synapse identification and neurite tracing. (**a**) Volume reconstruction of a spiny dendrite (green) in the striatum and 74 incident synaptic boutons (randomly colored) from a high-magnification SBEM data set (voxel size: 10 × 10 × 30 nm^3; for stack data, see **Supplementary Video 1**). (**b**) *xy* and *yz* cross-sections through a typical asymmetrical synapse onto a spine head. (**c**) *xy* section across a typical symmetrical synapse onto the dendritic shaft (for stack data, see **Supplementary Data**). (**d**) Presynaptic-bouton volume versus contact area. (**e**) Synapses identified by all three annotators (blue), two annotators (mauve) and only a single annotator (red) together with one skeleton tracing. Inset, cross-section through a synapse found by two tracers. Note the ill-defined vesicle cloud. (**f**) 20-fold skeletonization of the dendrite shown in **a**. (**g**–**i**) RESCOP vote histogram (**g**), estimated edge-detection probability $p(p_e)$ distributions for cerebral cortex (ctx), external capsule (ec) and striatum (str) (**h**), and mean error-free path length as a function of annotator redundancy (**i**). Scale bars, 1 µm.

less prominent in our preparations than in sections post-stained with uranyl acetate and lead[25,26] probably because we used only osmium and no other heavy metal that stains synapses.

To quantify traceability, we used the same neurite that had been used for the analysis of synapse detectability, another dendrite in the somatosensory cortex, and an unmyelinated axon in the external capsule and traced each of them 20 times, with each annotator blind to what the other annotators had done (**Fig. 3f**). Redundant-skeleton consensus procedure (RESCOP) analysis[27] of these tracings (**Fig. 3g–i**) showed disagreement rates between tracers of 0.46% in somatosensory cortex, 0.18% in the external capsule and 0.24% in striatum—substantially less than the 2–5% seen in a recent study in the retina[27]. Mean error-free path lengths after consolidation of the 20 tracings were estimated to be 1.12 mm and 2.22 mm for dendrites in somatosensory cortex and in the striatum, respectively, and 84.3 mm for the axon in the external capsule.

To obtain more information about axonal error rates, we selected 11 of the axons that made synaptic contact with the volume-reconstructed dendrite in the striatum (**Fig. 3a**) and traced each of them twice to the boundary of the data set. In only 1 out of 22 cases did the exit points disagree, which, given an average length of those tracings of 14.0 µm, translates into an error rate of 0.32% per micrometer, or about 0.054% per edge.

Finally, we tested human annotator ability to reconstruct neurites that run within and between different brain regions. To this end we acquired a stack at a resolution of 40-nm pixel size and 50-nm slice thickness that started in layer 4 of somatosensory cortex and ended in the striatum (**Supplementary Fig. 4**). The stack comprises 30,464 slices and contains 2,151 neuronal and

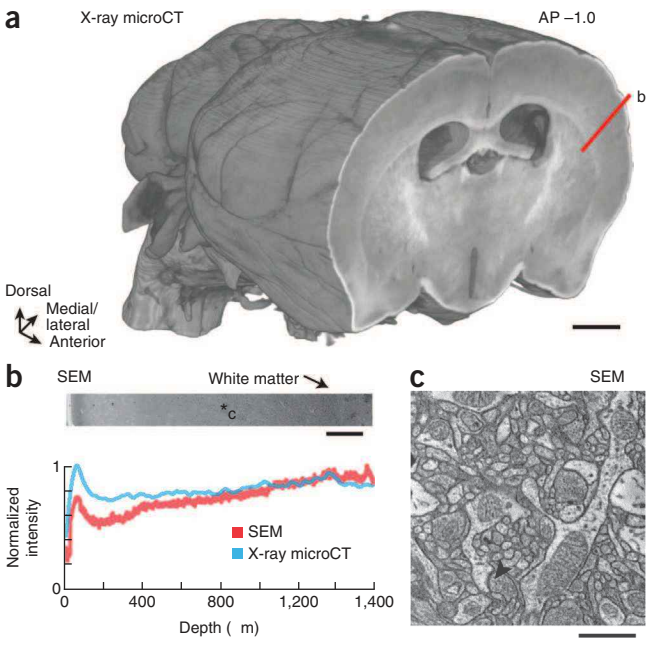

Figure 4 | Staining density and sample integrity can be assessed using X-ray microCT. (**a**) Three-dimensional rendering of a BROPA-prepared brain imaged by microCT (8.0-µm voxel size) and virtually sectioned coronally at approximately 1.0 mm posterior to bregma. (**b**) SEM image from a smoothed block face corresponding to the area indicated by the red line in **a**, and the intensity-versus-depth profiles for microCT (blue) and block-face SEM (red). (**c**) High-resolution SEM image (10-nm pixel size, 2.8 kV, 90 pA, 11.2 e$^-$/nm^2) of the block face at the location indicated by the asterisk in **b**. The arrowhead indicates an asymmetric synapse onto a spine head. Scale bars, 1 mm (**a**), 100 µm (**b**) and 2 µm (**c**).

1,174 glial somas, which were visually identified in the volume on the basis of nuclear profile and proximal-neurite morphology. We randomly selected a subset of 381 neurons for manual tracing (**Supplementary Fig. 4b**). Of these, 277 (72.7%) had neurites that reached the boundary of the imaged volume on at least one occasion. Additional tracings were made of external-capsule myelinated axons, some of which ascended into the overlying somatosensory cortex (**Supplementary Fig. 4b**). The capacity to distinguish between myelinated and unmyelinated axons allowed us to make some unexpected observations, such as completely unmyelinated ascending collaterals from a myelinated cortical neuron (**Supplementary Fig. 4c**), adding to the diversity of myelination patterns described previously[28].

Staining uniformity and the absence of internal distortions or structural damage can be assessed nondestructively down to the single-digit micrometer spatial scale by high-resolution X-ray microcomputed tomography (microCT; **Fig. 4a** and **Supplementary Video 4**), which exhibits an image contrast similar to that of SEM (**Fig. 4b**). This allowed us to quickly test an embedded brain for defects and distortion before deciding whether to finish preparing it for electron microscopy. Occasionally cracks were seen in BROPA-prepared brains (**Supplementary Fig. 5** and **Supplementary Video 4**). These cracks were generally devoid of epoxy; they likely developed after the curing step as the sample was cooling and could thus be minimized by cooling the sample more slowly. Furthermore, it is very likely that one can pursue even small processes across clean cracks[29]. The ability to test for defects early will reduce the chance that a whole-brain high-resolution electron microscopy scan will fail to provide a complete data set because a hidden defect emerges late during an acquisition, which may take a year or more.

DISCUSSION

BROPA-prepared brains appear to meet all the requirements for a complete neural circuit reconstruction of the whole mouse brain. They can be cut by a diamond knife, which results in a surface quality appropriate for serial block-face imaging (**Fig. 2** and **Supplementary Videos 1**–**3**) and presumably also for the Automatic Tape-collecting (Lathe) Ultra-Microtome[30], AT(L)UM, or the "hot-knife" method[29]. Throughout the brain the tissue, ultrastructure is preserved well enough to identify chemical synapses and trace even the thinnest neurites, such as spine necks and small-caliber axons (**Fig. 3**). Although error rates for dendrites appear to be substantially above those for axons, both dendrites and axons should be traceable when consolidation between annotators is used with mean distances between errors that are larger than their extent reached from the soma (**Fig. 3i**). This makes it plausible that entire cells can be reconstructed with reasonable accuracy. Even the purely manual reconstruction of a limited number of cells should provide insights into computational questions, in particular because it is possible to reliably jump from one cell to another that is synaptically connected, which is not an option when using light microscopy–based reconstructions. By starting from a number of somata in a particular area and tracing their axons, one could perform any number of virtual injections (in a single brain) and thus determine not only which areas these cells project to but also which cells they connect to synaptically. The morphological parameters of the contacts would be readily available, unlike with trans-synaptic virus-based techniques. Although it is unrealistic to expect that a whole mouse brain will ever be connectomically reconstructed by purely manual tracing, a combination of automated segmentation and manual proofreading might succeed. Current automatic reconstruction techniques show error rates that are orders of magnitude from what will ultimately be needed, but it may be the availability of a whole-brain data set that will provide the incentive needed to develop much more reliable analysis techniques.

METHODS

Methods and any associated references are available in the online version of the paper.

Note: Any Supplementary Information and Source Data files are available in the online version of the paper.

ACKNOWLEDGMENTS

We thank K.L. Briggman, K. Hayworth and S.K. Mikula for discussions; J. Bollmann, J. Kornfeld and S.K. Mikula for comments on the manuscript; A. Scherbarth, S.K. Mikula, M. Mueller, C. Roome, R. Shoeman, B. Titze and J. Tritthardt for technical support, D. Zeidler for providing the multi-beam images, J. Kornfeld, I. Sonntag, and F. Svara for help with traceability analysis and tracer organization; and D. Bornhorst, A. Greiss, U. Häusler, J. Hügle, A. Ivanova, F. Kaufhold, C. Kehrel, P. Kroemer, J. Loeffler, L. Muenster, S. Oberrauch, J. Phillip, N. Reisert, N. Scherer, F. Scheu and M. Webeler for tracing neurites. This work was supported by the Max Planck Society.

AUTHOR CONTRIBUTIONS

S.M. and W.D. conceived of the project and wrote the paper. S.M. designed the study, carried out the experiments and analyzed the data.

COMPETING FINANCIAL INTERESTS

The authors declare competing financial interests: details are available in the online version of the paper.

1. Denk, W., Briggman, K.L. & Helmstaedter, M. Structural neurobiology: missing link to a mechanistic understanding of neural computation. *Nat. Rev. Neurosci.* **13**, 351–358 (2012).
2. Lichtman, J.W. & Denk, W. The big and the small: challenges of imaging the brain's circuits. *Science* **334**, 618–623 (2011).
3. Jarrell, T.A. *et al.* The connectome of a decision-making neural network. *Science* **337**, 437–444 (2012).
4. Briggman, K.L., Helmstaedter, M. & Denk, W. Wiring specificity in the direction-selectivity circuit of the retina. *Nature* **471**, 183–188 (2011).
5. Bock, D.D. *et al.* Network anatomy and *in vivo* physiology of visual cortical neurons. *Nature* **471**, 177–182 (2011).
6. Knott, G., Marchman, H., Wall, D. & Lich, B. Serial section scanning electron microscopy of adult brain tissue using focused ion beam milling. *J. Neurosci.* **28**, 2959–2964 (2008).
7. Mikula, S., Binding, J. & Denk, W. Staining and embedding the whole mouse brain for electron microscopy. *Nat. Methods* **9**, 1198–1201 (2012).
8. Li, A. *et al.* Micro-optical sectioning tomography to obtain a high-resolution atlas of the mouse brain. *Science* **330**, 1404–1408 (2010).
9. Willingham, M.C. & Rutherford, A.V. The use of osmium-thiocarbohydrazide-osmium (OTO) and ferrocyanide-reduced osmium methods to enhance membrane contrast and preservation in cultured cells. *J. Histochem. Cytochem.* **32**, 455–460 (1984).
10. Deerinck, T.J. *et al.* Enhancing serial block-face scanning electron microscopy to enable high resolution 3-D nanohistology of cells and tissues. *Microsc. Microanal.* **16**, 1138–1139 (2010).
11. Zweens, J., Frankena, H., Rispens, P. & Zijlstra, W.G. Determination of extracellular fluid volume in the dog with ferrocyanide. *Pflugers Arch.* **357**, 275–290 (1975).
12. Van Harreveld, A., Crowell, J. & Malhotra, S.K. A study of extracellular space in central nervous tissue by freeze-substitution. *J. Cell Biol.* **25**, 117–137 (1965).
13. Thorne, R.G. & Nicholson, C. *In vivo* diffusion analysis with quantum dots and dextrans predicts the width of brain extracellular space. *Proc. Natl. Acad. Sci. USA* **103**, 5567–5572 (2006).

14. Van Harreveld, A. in *The Structure and Function of Nervous Tissue* (ed. Bourne, G.H.) Ch. 10, 447–511 (Academic Press, 1972).
15. Cragg, B. Preservation of extracellular space during fixation of the brain for electron microscopy. *Tissue Cell* **12**, 63–72 (1980).
16. Rivlin, P.K. & Raymond, P.A. Use of osmium tetroxide-potassium ferricyanide in reconstructing cells from serial ultrathin sections. *J. Neurosci. Methods* **20**, 23–33 (1987).
17. Karnovsky, M.J. Use of ferrocyanide-reduced osmium tetroxide in electron microscopy. *Proc. Am. Soc. J. Cell Biol.* **51**, 146a (1971).
18. Alexander, R., Ko, E.C.F., Mac, Y.C. & Parker, A.J. Solvation of ions. XI. Solubility products and instability constants in water methanol, formamide, dimethylformamide, dimethylacetamide, dimethyl sulfoxide, acetonitrile, and hexamethylphosphorotriamide. *J. Am. Chem. Soc.* **89**, 3703–3712 (1967).
19. Denk, W. & Horstmann, H. Serial block-face scanning electron microscopy to reconstruct three-dimensional tissue nanostructure. *PLoS Biol.* **2**, e329 (2004).
20. Bahr, G.F. Osmium tetroxide and ruthenium tetroxide and their reactions with biologically important substances: electron stains III. *Exp. Cell Res.* **7**, 457–479 (1954).
21. Hayat, M.A. *Principles and Techniques of Electron Microscopy: Biological Applications* 4th edn. (Cambridge Univ. Press, 2000).
22. Greedan, J.E., Willson, D.B. & Haas, T.E. Metallic nature of osmium dioxide. *Inorg. Chem.* **7**, 2461–2463 (1968).
23. Eberle, A.L. *et al.* High-resolution, high-throughput imaging with a multibeam scanning electron microscope. *J. Microsc.* doi:10.1111/jmi.12224 (27 January 2015).
24. Titze, B. & Denk, W. Automated in-chamber specimen coating for serial block-face electron microscopy. *J. Microsc.* **250**, 101–110 (2013).
25. Pfenninger, K.H. The cytochemistry of synaptic densities. I. An analysis of the bismuth iodide impregnation method. *J. Ultrastruct. Res.* **34**, 103–122 (1971).
26. Tapia, J.C. *et al.* High-contrast en bloc staining of neuronal tissue for field emission scanning electron microscopy. *Nat. Protoc.* **7**, 193–206 (2012).
27. Helmstaedter, M., Briggman, K.L. & Denk, W. High-accuracy neurite reconstruction for high-throughput neuroanatomy. *Nat. Neurosci.* **14**, 1081–1088 (2011).
28. Tomassy, G.S. *et al.* Distinct profiles of myelin distribution along single axons of pyramidal neurons in the neocortex. *Science* **344**, 319–324 (2014).
29. Hayworth, K.J. *et al.* Ultrastructurally smooth thick partitioning and volume stitching for large-scale connectomics. *Nat. Methods* doi:10.1038/nmeth.3292 (16 February 2015).
30. Hayworth, K.J., Kasthuri, N., Schalek, R. & Lichtman, J.W. Automating the collection of ultrathin serial sections for large volume TEM reconstructions. *Microsc. Microanal.* **12**, 86–87 (2006).

ONLINE METHODS

Animals used. We used a total of 146 adult (16–24 weeks old) wild-type (C57BL/6) male mice. We anesthetized the mice with isoflurane (Baxter) inhalation and then transcardially perfused them with fixative solution. We prepared three whole brains (WB104, WB118, and WB139) using the final version of the BROPA procedure. These brains were then used to evaluate ultrastructural preservation and to assess stain quality, synapse identification and neurite traceability. We used the remaining animals for the development of the staining protocol and the optimization of parameters. All procedures were approved by the Regierungspraesidium Karlsruhe and were in accordance with the laws of animal experimentation issued by the German federal government.

Sample screening. We purchased all reagents from Sigma-Aldrich unless otherwise indicated. We cut small cuboidal samples (1–2 mm per side) with a scalpel from the telencephalons of brains that had been fixed under ECS-preserving conditions (see below). We controlled the temperature by placing samples in a refrigerator (2 °C), in the ambient conditions of the lab or in an oven set to 50 °C. Incubations were done in 2-ml centrifuge tubes, which were replaced after each of the staining steps but not after rinse, dehydration or infiltration steps. For curing, we placed the samples into silicone molds and incubated them for 24 h in an oven at 60 °C. After trimming and smoothing the surface to be assessed, we acquired overviews of the samples using SEM (FEI QuantaFEG 200 or Zeiss Merlin), typically at a resolution of 440 nm, 4-keV landing energy and 150-pA beam current. We tested the effectiveness of various additional chemicals by incubating samples that had previously been incubated in reduced osmium (1.5 h in 40 mM OsO_4, 35 mM $K_4Fe(CN)_6$, 100 mM sodium cacodylate buffer, CB) for 2 h in a filtered, unbuffered, aqueous solution containing 1% (w/v) of the chemical. When the solubility was <1%, a filtered saturated solution was used. We rinsed samples with H_2O for 10 min, incubated them in an aqueous solution of 40 mM OsO_4 for 2 h and then dehydrated, embedded, trimmed and surface-smoothed them before imaging on a SEM.

BROPA sample preparation. The protocol used for the whole-brain samples (**Fig. 1b**) consisted of a series of immersion steps following the initial aldehyde perfusion. After anesthesia, the mouse was placed supine, and a horizontal cut was made into the upper abdomen. First the diaphragm was cut, then the ribs were cut laterally and the chest flap was folded back using a hemostat. The heart was exposed and held in place using curved, serrated forceps (Moria MC31, Fine Science Tools) while a 23-gauge cannula that was connected to the perfusion system was carefully inserted into the caudal end of the left ventricle and secured using a micro-serrefine (Model 18055-05, Fine Science Tools). The right auricle was pierced with fine scissors in order to allow the perfusate to emerge. The perfusion system consisted of a 30-ml syringe (Becton Dickinson) filled with an aqueous solution containing 250 mM (2.5% w/v) glutaraldehyde (GA, Serva), 100 mM CB (pH 7.4, Serva) and 120 mM (4% w/v) sucrose (Serva). The solution was made fresh about 30 min before the experiment started and was at room temperature (~20 °C). Perfusion was started by depressing the plunger of the syringe and keeping an approximately constant force on the plunger, resulting in a flow rate of about 0.5 ml/s, and continued until at total of 30 ml had been perfused through the animal. We were careful to initiate aldehyde perfusion <20 s after severing the diaphragm. Note that the protocol was identical to the one used by Cragg[15] with the following modifications: we (i) did not use gravity to drive perfusion, (ii) did not increase the pressure gradually but instead applied the full force to the plunger immediately, and (iii) did not precede the aldehyde perfusion with a rinse because we found that this led to variable preservation of the ECS.

After the perfusion, we decapitated the mouse and removed the muscle and skin tissue around the cranium using small scissors (Hardened Fine Scissors, Fine Science Tools). Using forceps, we removed the remaining two or three vertebrae and finally the skull by carefully breaking off small bone fragments, starting from the opening of the spinal columns, until the brain was completely exposed. During this procedure we kept the brain wet by periodically applying fixative solution. We cut the cranial nerves with small scissors before removing the brain and placing it, together with a number of other brains, into a glass container that was filled with a solution that was identical to what was used for perfusion fixation. The glass container was transferred to the refrigerator (2 °C) and kept there for 48–72 h without agitation. Brains were then rinsed (five cycles, 8–12 h each) by replacing the incubating solution with one that was identical and also kept at 2 °C but did not contain GA. After the last rinse cycle, the brains were stored in the rinse solution for up to 2 weeks. During all subsequent steps the solution volumes were 50 ml and the samples were kept at room temperature in the dark, gently agitated using a 3D gyratory rocker (SSL3, Stuart) at 10 r.p.m.

The first step in the staining procedure was to transfer the brain to a 50-ml centrifuge tube filled with an aqueous solution containing 40 mM OsO_4 (Electron Microscopy Sciences), 35 mM $K_4Fe(CN)_6$, 100 mM CB (pH 7.4) and 2.5 M formamide.

After 96 h, we transferred the brain to another tube (without a rinse step) containing an aqueous solution of 40 mM OsO_4 and 100 mM CB (pH 7.4). 72 h later we replaced the solution with 100 mM CB. After 4 h we transferred the brain to a tube containing an unbuffered aqueous solution of 320 mM pyrogallol at a pH of 4.1. Note that buffering the pyrogallol solution to a more alkaline pH with CB resulted in reduced membrane contrast (data not shown). The pyrogallol solution was not made up fresh for each experiment but rather came from an aqueous 1.28 M stock solution that was prepared at least 6 weeks earlier and kept in the dark at 20 °C. It has a translucent ruby color, presumably owing to larger polyhydroxy phenols formed by oxidization[31] (using ambient O_2). After 72 h we replaced the pyrogallol solution with 100 mM CB for 4 h. We then transferred the brain to another tube containing an unbuffered aqueous solution of 40 mM OsO_4 and kept it there for 96 h.

The dehydration incubations were 18–24 h each. Before the first step we transferred the brain to a new tube, where it remained for all subsequent steps. The concentrations (all v/v) were 10%, 25%, 50%, 75% and 100% ethanol balanced with water followed by 100%, 75%, 50%, 25% and 0% propylene oxide balanced with epoxy. The epoxy formulation, a modification from Spurr's[32], was: 10 g vinylcyclohexene dioxide (VCHD or ERL-4206), 20 g nadic methyl anhydride (NMA, Electron Microscopy Sciences) and 0.45 g dimethylaminoethanol (DMAE, Serva). The acetic anhydride, nonenyl succinic anhydride (NSA), was replaced by NMA, which among the anhydrides commonly used as hardeners (NMA, NSA

and dodecenyl succinic anhydride (DDSA)) yields the hardest blocks while also penetrating well. We used only VCHD rather than a mixture of VCHD and diglycidyl ether of polypropylene glycol (D.E.R. 736) because the latter reduces block hardness[32]. For epoxy polymerization the brain was placed into a custom-made rectangular silicone mold of dimensions 7 mm × 10 mm × 18 mm and cured at 60 °C for 48 h.

X-ray microCT imaging. Images were collected by SCANCO Medical AG with a microCT scanner (μCT 100, SCANCO Medical AG) in air using absorption contrast, 90-kV energy, 89-μA intensity, 0.1-mm Cu filter, 20-mm field of view, 2,550 × 2,550 × 1,000 image matrix, 8.0-mm scan length, 900-ms integration time, two-frame averaging, 1,500 180° projections, 8.0-μm voxel size and 5.5-h scan time. X-rays from a microfocus X-ray source were passed through the epoxy-embedded BROPA-prepared brain, and projections were collected by a high-resolution charge-coupled device (CCD) detector.

SEM imaging. First the posterior part of the polymerized epoxy block containing the whole brain was trimmed using a rotary sample trimmer (EM Trim, Leica) until the spinal cord was exposed. The posterior surface of the block was then glued to an aluminum cylinder that was 10 mm in diameter and 16 mm high. Silver-filled conductive epoxy (CircuitWorks silver epoxy, Conrad) was used to provide a current path to ground (see below). Then the anterior portion of the block was removed up to about bregma −0.34 using the rotary trimmer. The cross-sectional surface was then smoothed on a ultramicrotome (Ultracut UCT, Leica). The diamond knife used (histo Jumbo, Diatome) was 8 mm wide and was set to a clearance angle of 3.5°. The cutting speed was 1.0 mm/s. The section thickness was generally 100 nm but in cases of chatter formation was manually varied between 70 and 100 nm to eliminate the chatter. Then the sample was introduced into a scanning electron microscope with a field-emission cathode (QuantaFEG 200, FEI or Merlin, Zeiss). Back-scattered electrons (BSEs) were detected using a silicon-diode detector (AXUV, International Radiation Detectors) connected to a low-noise custom-built current amplifier (MPIMF electronics shop). The sample was mounted onto the SEM sample stage using a custom stage adaptor. An overview image comprising about 100 overlapping tiles that covered the entire coronal cross-section of the brain was then taken at a working distance of about 10 mm, a landing energy of 4 keV and a spot size of 3.5 (~150 pA). The frame size for each tile was 2,048 × 1,768 pixels, which at a pixel pitch of 440 nm resulted in a field of view of 900 μm × 780 μm. The placement of the tiles in the composite overview images was performed using the stage coordinates.

After identifying the locations where the subsamples for SBEM acquisition were to be extracted from the brain, we imaged each of those locations at a pixel pitch of 40 nm for several minutes. This generated marks visible to the naked eye that were then used to guide subsample extraction, which proceeded exactly as previously described[7]. Before SBEM imaging, each subsample was glued with silver-filled conductive epoxy to a custom pin and trimmed to a size of about 0.5 mm using the rotary trimmer. Then each sample was coated with gold (~30 nm thick) using a thermal evaporator (Bal-TEC MED 020) before we mounted it into the SBEM (custom built by the MPIMF shops). During stack acquisitions, slices were cut at 30-nm increments. SEM imaging was at 5.8-mm working distance, 2.8-keV landing energy, 2-μs pixel dwell time, and spot size of 3.0 (for somatosensory cortex and the external capsule) or 3.5 (for striatum), corresponding to 90-pA (11.2 e^-/nm^2) and 150-pA (18.7 e^-/nm^2) beam current, respectively. The frame size was 2,048 × 1,768 pixels, which resulted in a field of view of 20.5 μm × 17.7 μm. Optimal focus and stigmation were maintained during stack acquisition using iterative aberration-correction, the "heuristic algorithm"[33].

A different whole-brain sample was used to acquire the corticostriatal stack (**Supplementary Fig. 4**). In that case we removed the anterior part up to bregma 0.62 mm before smoothing the sample and taking an overview image. The subregion used for the stack was localized using cortical and white-matter landmarks that were visible to the naked eye, presumably owing to differential shrinkage of the sample in vacuum. The subvolume was isolated by using a circular saw–type cutter to first cut around the subvolume to a depth of 1 mm and then to undercut it until it started to vibrate visibly, and finally the subvolume was removed using a scalpel blade. After its removal from the block, the subsample, which was 2 mm long, was mounted on end onto a custom SBEM pin using conductive epoxy (CircuitWorks silver epoxy, Conrad). During the polymerization step (70 °C overnight), the sample was prevented from tilting or falling over by a piece of silicone tubing, which was subsequently removed. To avoid exhausting its range, we reset the sample advance mechanism and correspondingly moved up the sample in its holder several times after cutting about 8,000 slices each time, at which point we also blew away the cutting debris with a stream of dry nitrogen gas. During two of these resets, the sample was removed from the SBEM and retrimmed to avoid exceeding the area that can be cut with the SBEM microtome. After reinserting the sample, we repositioned it laterally and rotationally using reference images taken before and after the reset. After that the diamond knife was brought to within a few micrometers of the surface by using the knife edge and its reflection on the sample surface. The knife was then repeatedly swept across the surface; each time, the gap was reduced by 50 nm until very fine pieces of debris on the surface were engaged by the knife edge. The sample was retracted by 200 nm and the microtome was introduced into the SEM chamber, which was then pumped down. The cutting cycle was started, with removal of material from the surface starting after at most ten cycles. The corticostriatal SBEM stack was acquired using a 40-nm pixel size, 50-nm slice thickness, 3.3-keV landing energy, spot size of 3.3, 5.8-mm working distance, 2-μs pixel dwell time, 130 pA and 1.0 e^-/nm^2. The total acquisition time was 28 d.

We registered SBEM data sets with subpixel precision using the following procedure. Pairwise interframe offsets were computed using FFT cross-correlation separately for five subregions (each 512 × 512 pixels) in the corners and the center of the image frame. Typically the shifts measured for different subregions were the same to within a few pixels. The disagreements between the shifts were substantially larger if one or more of the subregions contained debris. To prevent this from introducing errors in the alignment, we used median rather than mean shift values. By checking the image mean and variance, we could detect frames that contained large pieces of debris and exclude them from the registration process. To prevent coherent shifts due to fiber bundles oriented at an angle to the cutting-plane normal, we fitted a

doi:10.1038/nmeth.3361

fifth-order polynomial to the integrated shift values and used only the residuals to correct the image locations. After registration, the size for the corticostriatal stack was 4,382 × 3,435 × 30,464 voxels. Registered high-resolution SBEM data sets, but not the corticostriatal stack, were cropped to 1,024 × 1,024 × 1,024 voxels for traceability analysis.

Traceability analysis. For the corticostriatal data set, all cell nuclei were manually identified and classified as neuronal, glial or other. For each of the high-magnification SBEM data sets (somatosensory cortex, external capsule and striatum), we selected a planar subregion from the center, identified all processes in an unbiased manner using the disector method[34,35], and then randomly selected 25 of these to be traced independently by five trained undergraduate tracers using Knossos (http://www.knossostool.org/). The 25 quintuple tracings were inspected, and the most highly branched tracing was selected to be traced an additional 20 times.

Skeleton consolidation was performed with the RESCOP method[27] using custom Matlab code (**Supplementary Software**). Votes for the edge e_{ij} (in tracing i) were determined as previously described[27] except that node-skeleton distances were calculated by first subsampling the skeleton (100-nm steps) and then using the minimum of the node-to-subsampling-point distances. The edge-detection probability distribution, $p(p_e)$, was approximated by 51 uniformly distributed triangular basis functions (**Fig. 3h**) and was optimized by maximizing (using the Nelder-Mead simplex method) the probability that it generated the observed vote histogram. To reduce the sensitivity to vote noise, we averaged the $p(p_e)$ over 100 trials using the vote histogram with different Poisson noise added each time.

To set the parameters r_p and θ (the skeleton distance threshold), we used the following procedure: one neurite in each SBEM data set was traced by three individuals, who tried to come to a consensus among themselves. The remaining variability between the tracings was then due entirely to variability in intraneurite node placement. We then determined the lowest value of r_p (with θ set to 625/700 r_p) for which no errors were reported, finding values of 650, 400 and 1,000 nm for the cerebral cortex, external capsule and striatum high-resolution data sets, respectively.

Synapse identification. ITK-SNAP (http://www.itksnap.org/) was used for manual segmentation. Knossos (http://www.knossostool.org/) tracing software was used for skeletonization and synapse annotation. To detect matches, we went through all the synapses found by the primary (volume) annotator and then inspected the corresponding locations in the Knossos annotations of the two secondary annotators. Bouton volumes were computed from the volume segmentation by simply counting the voxels. The contact area was determined using the following procedure: the volume segmentations of bouton and dendrite were resampled to 30-nm isotropic voxels, and the exterior (i.e., surface) voxels of each bouton were identified. If the distance between an exterior bouton voxel and the dendrite was less than or equal to 3 voxels, then 900 nm^2 was added to the contact area. This procedure was repeated, using Matlab, for all surface voxels and all boutons.

31. Siegel, S.M. & Siegel, B.Z. Autoxidation of pyrogallol: general characteristics and inhibition by catalase. *Nature* **181**, 1153–1154 (1958).
32. Spurr, A.R. A low-viscosity epoxy resin embedding medium for electron microscopy. *J. Ultrastruct. Res.* **26**, 31–43 (1969).
33. Binding, J., Mikula, S. & Denk, W. Low-dosage maximum-a-posteriori focusing and stigmation (MAPFoSt). *Microsc. Microanal.* **19**, 38–55 (2013).
34. Gundersen, H.J.G. *et al.* The new stereological tools: disector, fractionator, nucleator and point sampled intercepts and their use in pathological research and diagnosis. *APMIS* **96**, 857–881 (1988).
35. Fiala, J.C. & Harris, K.M. Extending unbiased stereology of brain ultrastructure to three-dimensional volumes. *J. Am. Med. Inform. Assoc.* **8**, 1–16 (2001).

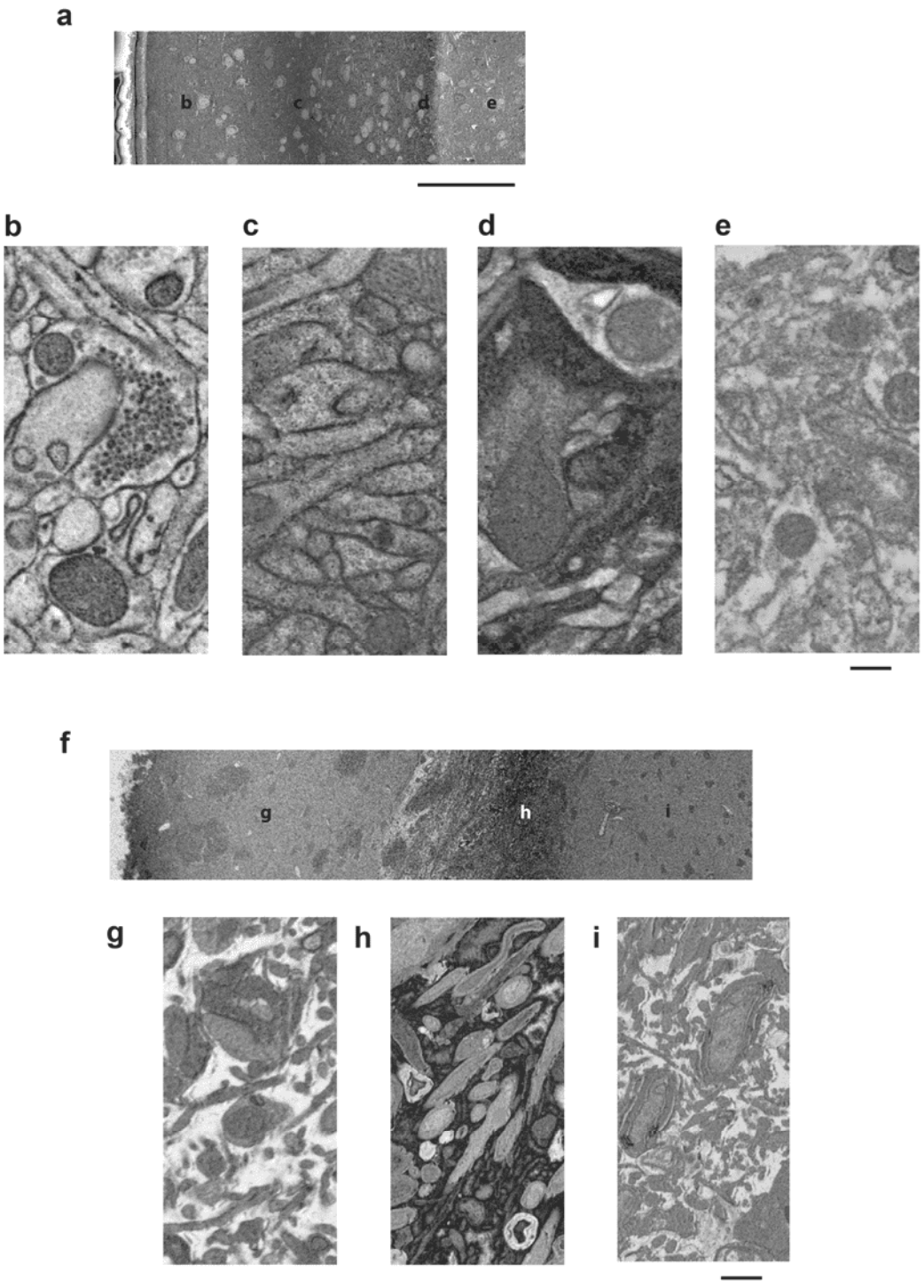

Supplementary Figure 1

ROTO staining and ultrastructural preservation over different depths.

SEM images for ROTO-prepared samples without, (**a**-**e**), and with, (**f**-**i**), extracellular space (ECS) preservation. Locations for high-resolution images indicated in the corresponding low-resolution scans. Imaging parameters are 440 nm pixel size, 2.8 kV, 100 pA, and 0.0064 e^-/nm^2 in **a** and **f**, 5 nm pixel size, 2.8 kV, 300 pA, and 600 e^-/nm^2 in **b**-**e**, and 10 nm pixel size, 2.8 kV, 100 pA, and 100 e^-/nm^2 in **g**-**i**. Scales bars are 100 μm in **a** and **f**, 250 nm in **b**-**e** and 500 nm in **g**-**i**.

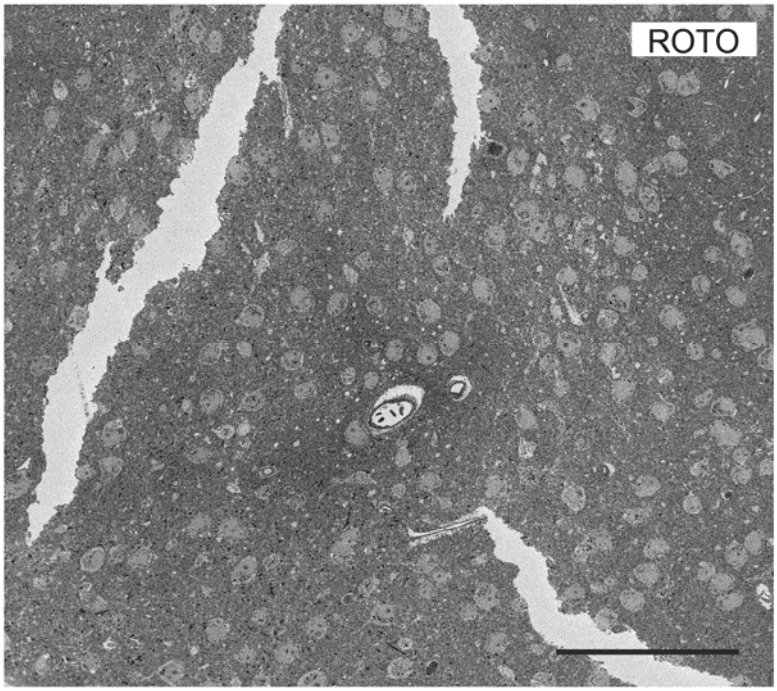

Supplementary Figure 2

Mechanical disruption in large ROTO-prepared samples.

SEM block-face image (220 nm pixel size, 2.8 kV, 100 pA, and 0.0256 e^-/nm^2) taken from a ROTO sample (with 10% formamide added to the reduced osmium step to increase stain penetration) prepared using an ECS-preserving perfusion medium. The scale bar corresponds to 100 μm.

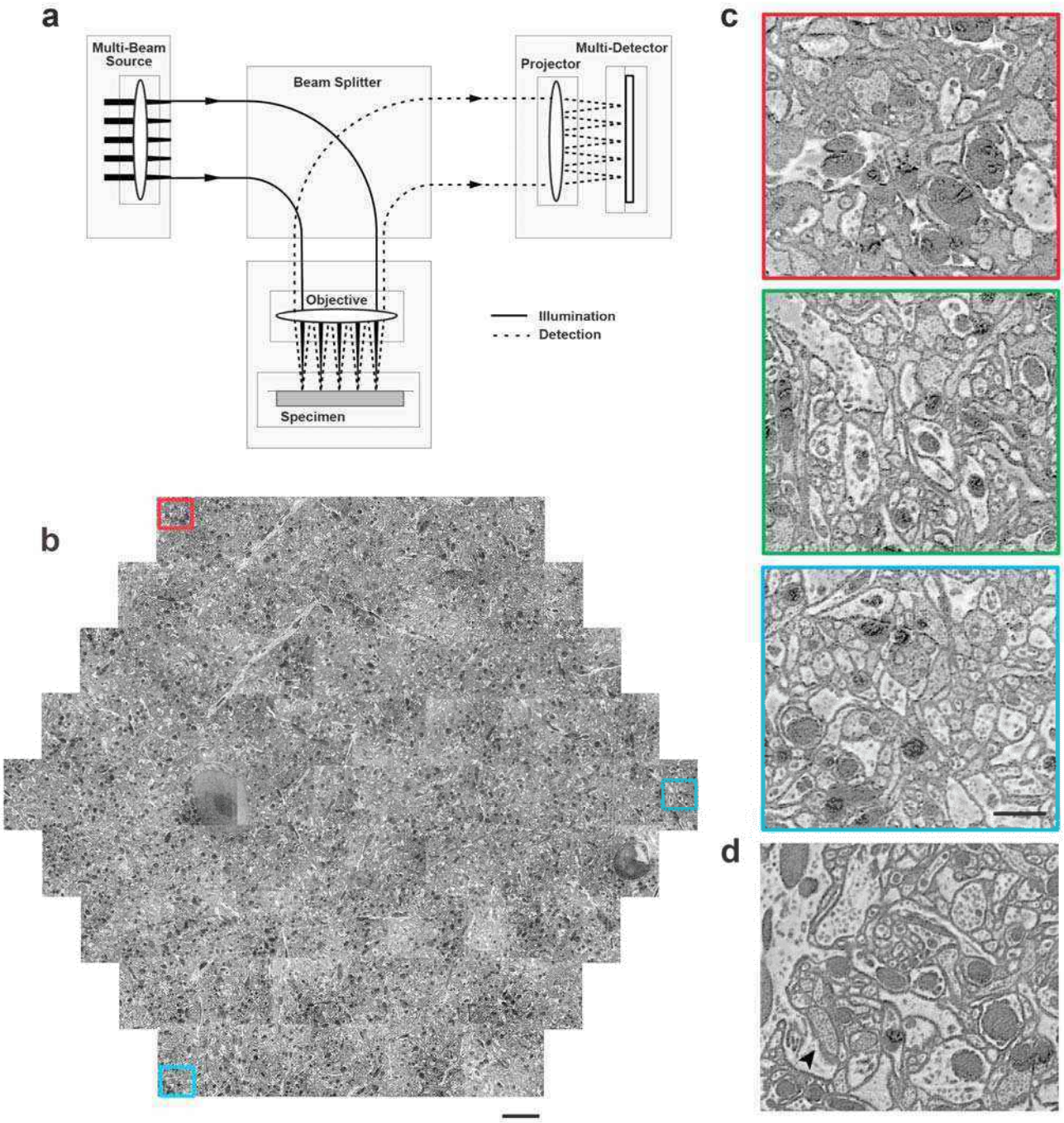

Supplementary Figure 3

Multibeam SEM imaging of a BROPA-prepared sample.

(**a**) Schematic of the prototype multi-beam microscope. (**b**) Image (3.8 nm pixel size, 430 pA, 100 ns pixel dwell time, 470 MPixel/s effective scan rate, 18.6 e^-/nm^2) of a block-face coated with a thin film of palladium to avoid charging. Each tile corresponds to an image taken by one of the 61 beams that scan the sample simultaneously. (**c**) Subregions as indicated in **b**. (**d**) Subregion from multi-beam SEM image acquired at high current (4.6 nm pixel size, 3 nA, 50 ns pixel dwell time, 755 MPixel/s effective scan rate, 44.2 e^-/nm^2). The sample is the same as in **b**. Asymmetric synapse onto a spine head (arrowhead). Scale bars are 10 μm in **b** and 1 μm in **c**. Scale bar in **c** also applies to **d**.

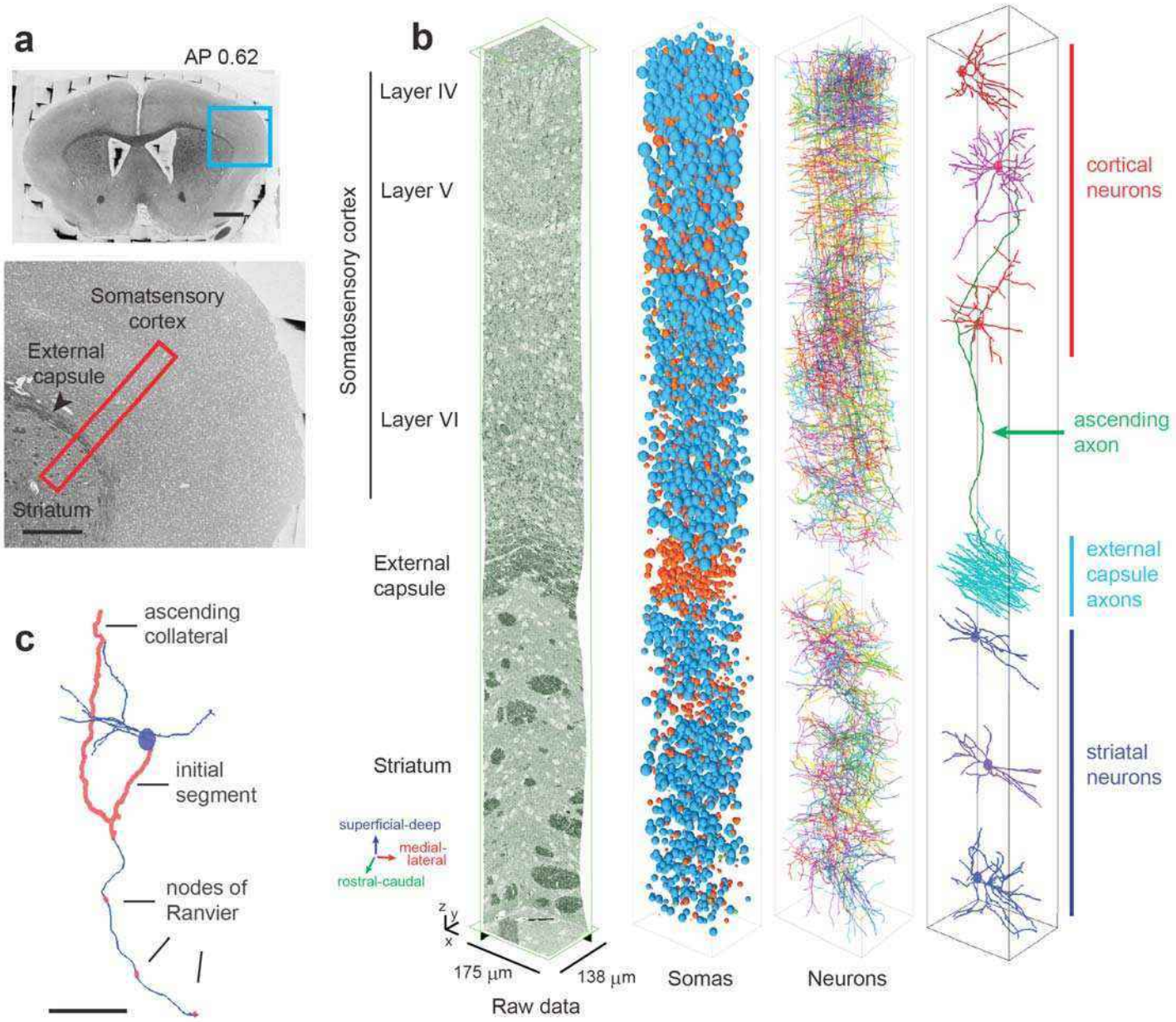

Supplementary Figure 4

Inter-areal SBEM and neurite traceability.

(**a**) Complete block-face SEM image (top, 440 nm pixel size, 4 kV, 150 pA, 0.0097 e^-/nm^2) of a BROPA brain and a higher-magnification view of the region of interest (bottom). The red rectangle shows the approximate extent of a continuous SBEM stack. The normal of the stack images is along the long axis of the rectangle. (**b**) From the left: surface view of aligned stack; manually identified neuronal (blue) and glial (red) nuclei; neurites emerging from 381 randomly-selected nuclei. 6 of 381 neurons (3 each in cortex and striatum) together with 100 randomly selected external-capsule axons. Note that one of them veers into cortex. (**c**) Single cortical cell with dendrites (thin blue lines), the initial segment and an ascending collateral (thick red, both unmyelinated), and the descending axon (thin blue line) with nodes of Ranvier (red). Scale bars are 1 mm in **a** (top), 500 µm in **a** (bottom), and 40 µm in **c**.

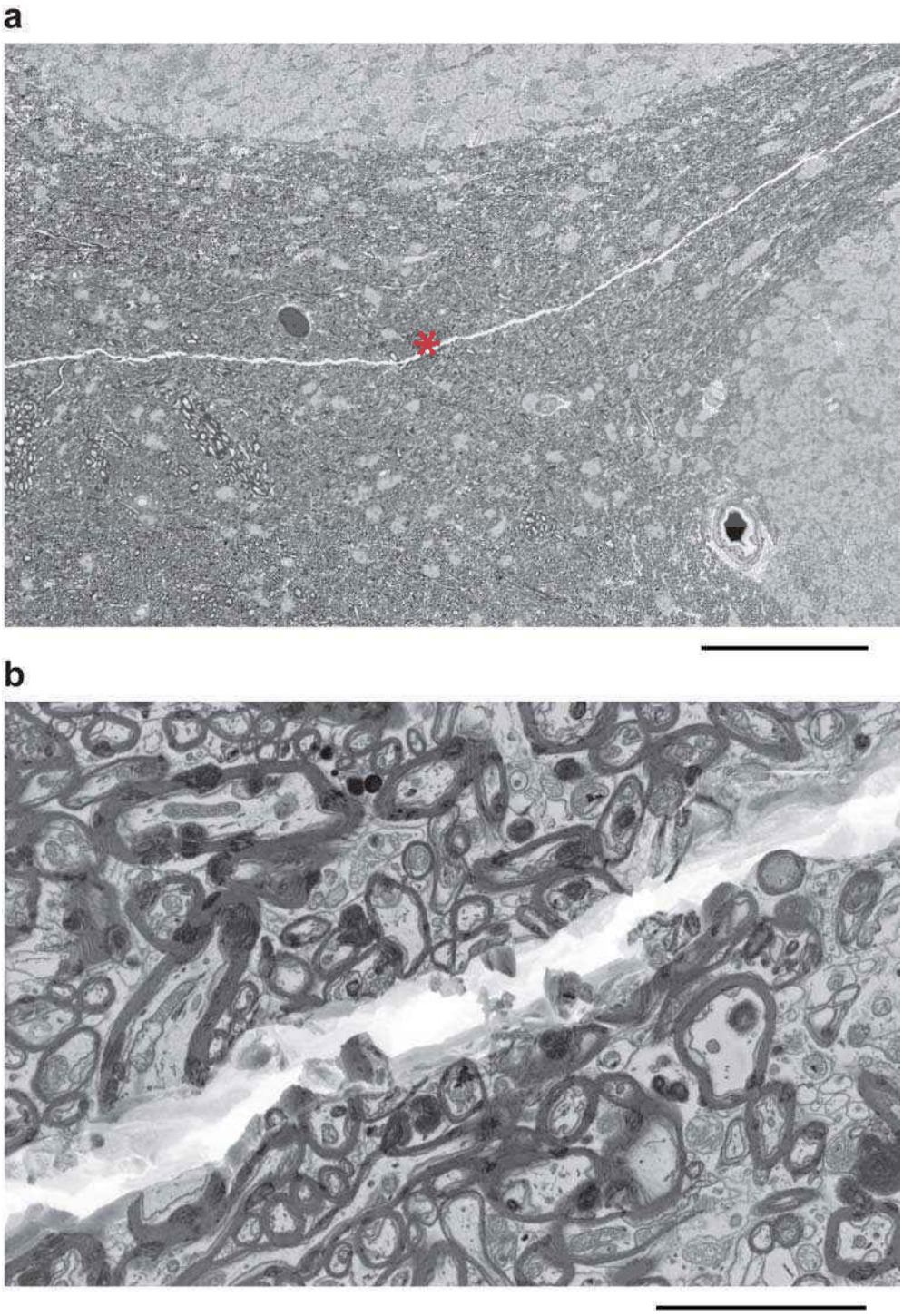

Supplementary Figure 5

Crack in BROPA sample.

(a) Cracks, generally devoid of epoxy, are occasionally observed in epoxy-embedded BROPA samples (see Supplementary Video 4). **(b)** High-magnification image of the red asterisk in **a**. Imaging parameters are 220 nm pixel size, 3.0 kV and 0.29 e^-/nm^2 in **a** and 10 nm pixel size, 3.0 kV and 140 e^-/nm^2 in **b**. Scale bars are 100 μm in **a** and 5 μm in **b**.

#